

QUANTUM OPTICS

Entangling microwaves with light

R. Sahu^{1*†}, L. Qiu^{1*†}, W. Hease^{1†}, G. Arnold¹, Y. Minoguchi², P. Rabl^{2,3,4,5}, J. M. Fink^{1*}

Quantum entanglement is a key resource in currently developed quantum technologies. Sharing this fragile property between superconducting microwave circuits and optical or atomic systems would enable new functionalities, but this has been hindered by an energy scale mismatch of $>10^4$ and the resulting mutually imposed loss and noise. In this work, we created and verified entanglement between microwave and optical fields in a millikelvin environment. Using an optically pulsed superconducting electro-optical device, we show entanglement between propagating microwave and optical fields in the continuous variable domain. This achievement not only paves the way for entanglement between superconducting circuits and telecom wavelength light, but also has wide-ranging implications for hybrid quantum networks in the context of modularization, scaling, sensing, and cross-platform verification.

The ability to manipulate and measure quantum mechanical properties such as quantum superpositions and entanglement in a variety of physical systems serves as the basis for the development of quantum technologies, for which the demonstration of quantum advantage with tens of superconducting qubits (1), an ultracoherent quantum memory with nuclear spins (2), and distributed quantum entanglement over tens of kilometers using optical photons (3) represents just a few of the highlights that have already been achieved. Combining these techniques (4–6) will enable the realization of general-purpose quantum networks in which remote quantum nodes capable of storing and processing quantum information seamlessly communicate with each other by distributing entanglement over optical channels (7). Aspects of this approach have already been adopted to connect and entangle various quantum platforms remotely. These involve single atoms, ions, atomic ensembles, quantum dots, rare-earth ions, and nitrogen-vacancy centers (8). However, such long-distance quantum connectivity is considerably more difficult to achieve with microwave-based platforms such as semiconductor spin qubits (9) or local cryogenic networks of superconducting circuits (10, 11), for which no natural interface to propagating optical photons is available.

To overcome this limitation, efforts are currently focused on the development of coherent quantum transducers between microwave and optical photons (12–17). Direct noiseless

conversion of a quantum state typically relies on a beam-splitter process in which a strong driving field mediates the conversion between weak microwave and optical signals. However, a deterministic channel based on direct transduction has exceptionally stringent requirements on conversion efficiency and added classical noise that are still out of reach. Alternatively, quantum states can be teleported over long distances (18–20) by first establishing an entangled state between microwave and optical photons. Because they are assisted by an error-free classical signal (21, 22), such teleportation-based communication channels are more tolerant to noise and losses, and their channel capacity is never zero as long as a finite amount of entanglement can be shared between the communicating nodes (22).

Theoretical outline and experimental setup

We generated and verified entanglement between microwave and optical fields in the continuous-variable domain (23) using an ultralow-noise cavity electro-optical device (21). Our device consists of a 5-mm-diameter,

150- μm -thick lithium niobate optical resonator placed inside a superconducting aluminum microwave cavity at a temperature of 7 mK, described in detail in (24). The microwave mode \hat{a}_e is electro-optically coupled to the colocated optical whispering gallery modes at $\omega_o/2\pi \approx 193.46$ THz through the Pockels effect (Fig. 1A). The microwave resonance frequency $\omega_e/2\pi$ is tuned to the optical free spectral range (FSR) of 8.799 GHz to realize a triply resonant system with interaction Hamiltonian:

$$\hat{H}_{\text{int}} = \hbar g_o \hat{a}_p \hat{a}_e^\dagger \hat{a}_o^\dagger + \text{h.c.} \quad (1)$$

where g_o is the vacuum electro-optical coupling rate and \hat{a}_p (\hat{a}_o) is the annihilation operator of the optical pump (Stokes) mode (25–28). Herein, we have ignored the interaction with the suppressed optical anti-Stokes mode \hat{a}_t (Fig. 1B) (29).

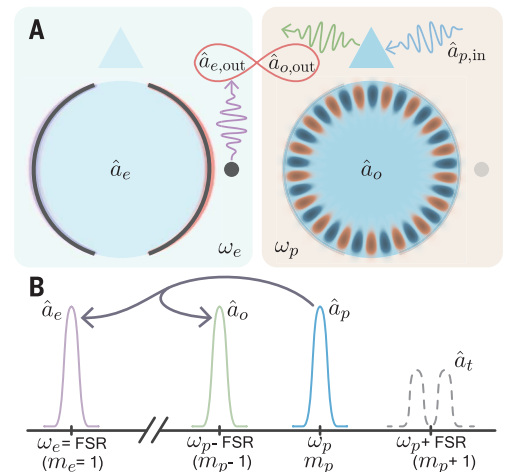
In this sideband suppressed situation, two-mode squeezing interaction was achieved with a strong resonant optical pump tone, yielding the simple effective Hamiltonian, $\hat{H}_{\text{eff}} = \hbar g_o \sqrt{\bar{n}_p} (\hat{a}_e^\dagger \hat{a}_o^\dagger + \hat{a}_e \hat{a}_o)$, where $\bar{n}_p = \langle \hat{a}_p^\dagger \hat{a}_p \rangle$ is the mean intracavity photon number of the optical pump mode. Entanglement between the out-propagating microwave and the optical field was generated through spontaneous parametric down-conversion (SPDC) below the parametric instability threshold ($C < 1$). Here, $C = 4\bar{n}_p g_o^2 / (\kappa_e \kappa_o)$ is the cooperativity with the vacuum coupling rate $g_o/2\pi \approx 37$ Hz and the total loss rates of the microwave and optical Stokes modes $\kappa_e/2\pi \approx 11$ MHz and $\kappa_o/2\pi \approx 28$ MHz. The required ultralow-noise operation for entanglement generation was achieved in the pulsed regime because of the slow heating of this millimeter-sized device despite the required high-power optical pump (24).

Establishing nonclassical correlations

We characterized the microwave and optical output fields using continuous variables, i.e.,

Fig. 1. Physical and conceptual mode configuration. (A) Simulated microwave (left) and optical (right) mode distribution with azimuthal number $m_e = 1$ and $m_o = 17$ (for illustration, experimentally $m_o \approx 20,000$).

Phase matching is fulfilled from the condition $m_o = m_p - m_e$, and entanglement is generated and verified between the out-propagating microwave field $\hat{a}_{e,\text{out}}$ and the optical Stokes field $\hat{a}_{o,\text{out}}$. (B) Sketch of the density of states of the relevant modes. Under the condition $\omega_p - \omega_o = \omega_e$, the strong pump tone in \hat{a}_p produces entangled pairs of microwave and optical photons in \hat{a}_e and \hat{a}_o through spontaneous parametric down-conversion. Frequency up-conversion is suppressed through hybridization of the anti-Stokes mode \hat{a}_t with an auxiliary mode.



¹Institute of Science and Technology Austria, am Campus 1, 3400 Klosterneuburg, Austria. ²Vienna Center for Quantum Science and Technology, Atominsttitut, TU Wien, 1040 Vienna, Austria. ³Walther-Meißner-Institut, Bayerische Akademie der Wissenschaften, 85748 Garching, Germany. ⁴Technische Universität München, TUM School of Natural Sciences, 85748 Garching, Germany. ⁵Munich Center for Quantum Science and Technology (MCQST), 80799 Munich, Germany.

*Corresponding author. Email: rsahu@ist.ac.at (R.S.); liu.qiu@ist.ac.at (L.Q.); jfink@ist.ac.at (J.M.F.)

†These authors contributed equally to this work.

‡Present address: Quandela SAS, 91120 Palaiseau, France.

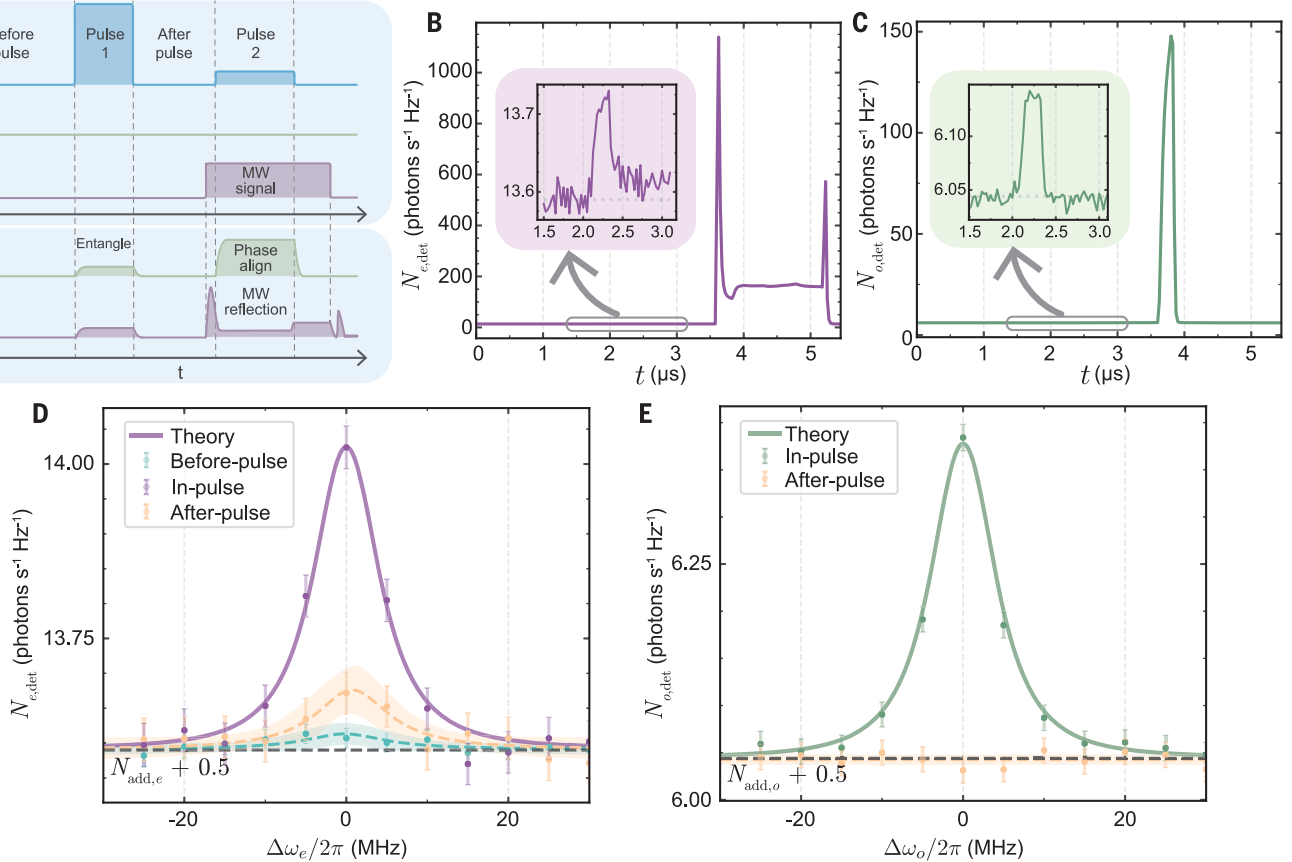


Fig. 2. Measurement sequence and noise powers. (A) Schematic pulse sequence of a single measurement. The optical pulse 1 is applied at ω_p and amplifies the vacuum (and any thermal noise) in the two modes \hat{a}_e and \hat{a}_o , thus generating the SPDC signals. One micro-second later, a second optical pump with ~ 10 times lower power is applied, together with a coherent microwave pulse at ω_e . The microwave photons stimulate the optical pump to down-convert, which generates a coherent pulse in the \hat{a}_o mode that is used to extract slow local oscillator phase drifts. (B and C) Measured output power from the \hat{a}_e and \hat{a}_o modes in units of photons per second in a 1-Hz bandwidth and averaged over a million experiments. The SPDC signals are shown in the insets, with the dashed gray lines indicating the

calibrated detection noise floor $N_{j,\text{add}} + 0.5$. (D) Corresponding microwave output power spectral density versus $\Delta\omega_e = \omega - \omega_e$ centered on resonance right before the entanglement pulse, during the pulse, and right after the pulse, as indicated in (A). Yellow and green dashed lines are fits to a Lorentzian function that yields the microwave bath occupancies before and after the entangling pulse. Error bars represent the 2σ statistical SE, and the shaded regions represent the 95% confidence interval of the fit. (E) Corresponding optical output power spectral density versus $\Delta\omega_o = \omega_o - \omega$ during and after the entanglement pulse, both normalized to the measured noise floor before the pulse. The in-pulse noise spectra in (D) and (E) are fit jointly with theory, which yields $C = 0.18 \pm 0.01$ and $\bar{n}_{e,\text{int}} = 0.07 \pm 0.03$.

the dimensionless quadrature pairs X_j and P_j (where $j = e, o$ for microwave and optics), which satisfy the canonical commutation relations $[X_j, P_j] = i$. A pair of Einstein-Podolsky-Rosen-type operators, $X_+ = \frac{1}{\sqrt{2}}(X_e + X_o)$ and $P_- = \frac{1}{\sqrt{2}}(P_e - P_o)$, were then constructed (30). The microwave and optical output fields are entangled if the variance of the joint operators is reduced below the vacuum level, i.e., $\Delta_{\text{EPR}} = \langle X_+^2 + P_-^2 \rangle < 1$. This is commonly referred to as the Duan-Simon criterion (31, 32). Here, the entanglement was established deterministically between the quadratures of two propagating bosonic modes and verified through the measured quadrature variances based on all collected data (33). This is in contrast to probabilistic entanglement in the single photon basis, which is established with finite probability only after

successful heralding from an auxiliary measurement (34).

For entanglement generation, we used a 250-ns-long optical pump pulse (≈ 154 mW, $C \approx 0.18$, $\bar{n}_p \approx 1.0 \times 10^{10}$) at a 2-Hz repetition rate (pulse 1 in Fig. 2A). The output optical signal was filtered through a Fabry-Perot cavity to reject the strong pump. The microwave output field was amplified by a high-electron-mobility transistor amplifier. Both outputs were down-converted to an intermediate frequency of 40 MHz with two local oscillators, and the four quadratures were extracted from heterodyne detection. Long-term phase stability between the two local oscillators was achieved by extraction of the relative phase drift by means of a second phase-alignment pump pulse that was applied $1 \mu\text{s}$ after each entanglement pulse,

together with a coherent resonant microwave pulse (Fig. 2A). This generated a high signal-to-noise coherent optical signal through stimulated parametric down-conversion and allowed for phase alignment in each individual measurement (29).

Figure 2, B and C, shows the time-domain power over 1 million averages for the on-resonance microwave and optics signal with a 40-MHz measurement bandwidth. The two insets show the microwave (optical) signal from spontaneous parametric down-conversion (SPDC) from pulse 1 (compare Fig. 2A) with an emission bandwidth of ~ 10 MHz. The larger signals during the second pump pulse are the reflected microwave pulse and the generated optical tone, and these were used for phase alignment. The off-resonance raw power measurements were rescaled to the

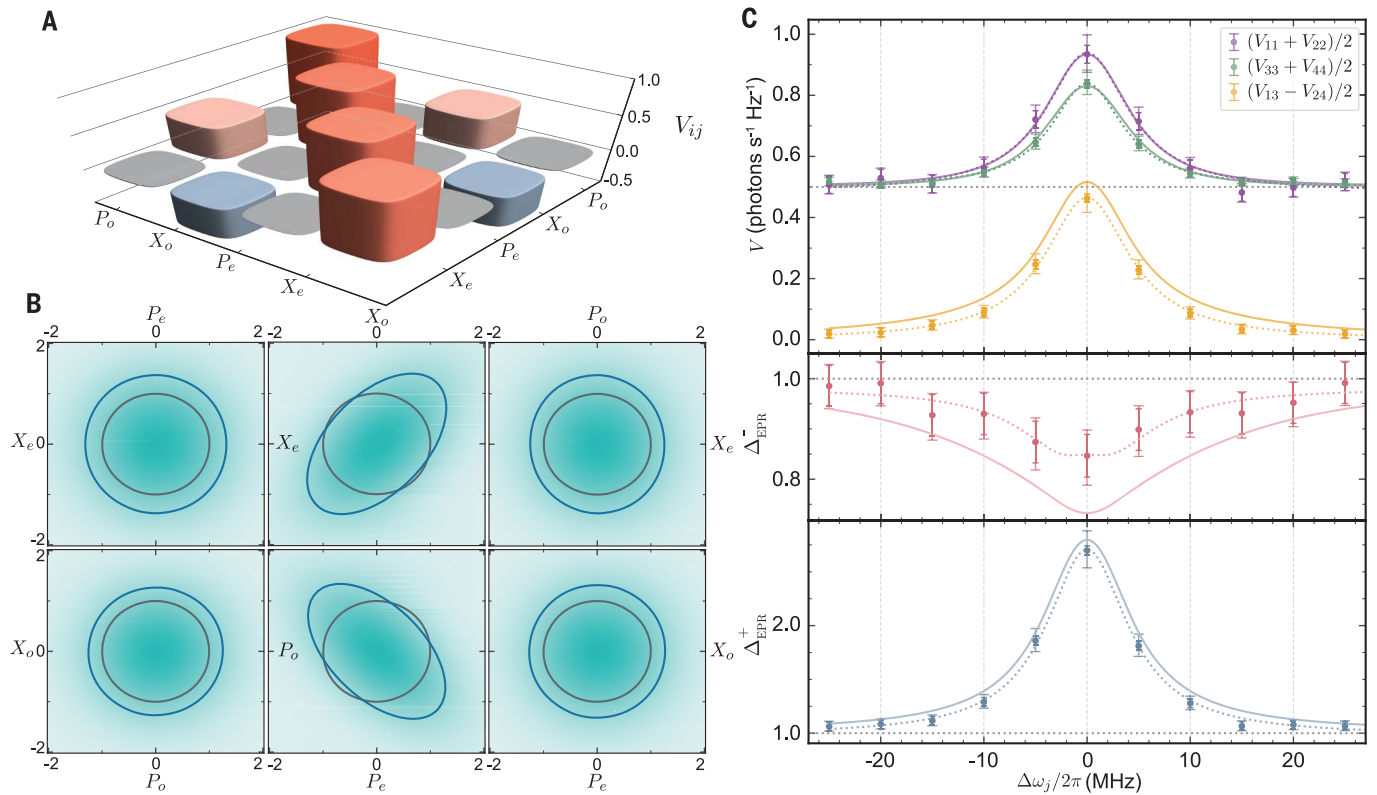


Fig. 3. Characterization of the two-mode squeezed state. (A) Measured covariance matrix V_{ij} in its standard form plotted for $\Delta\omega_j = 0$ based on 925,000 measurements. (B) Corresponding Wigner function marginals of different output quadrature pairs compared with vacuum. The contours in blue (gray) represent the $1/e$ fall-off from the maximum for the measured state (vacuum). The middle two plots show two-mode squeezing below the vacuum level in the diagonal and off-diagonal directions. (C) Top, measured average microwave output noise $\bar{V}_{11} = (V_{11} + V_{22})/2$ (purple), average optical output noise

$\bar{V}_{33} = (V_{33} + V_{44})/2$ (green), and average correlations $\bar{V}_{13} = (V_{13} - V_{24})/2$ (yellow) as a function of measurement detunings. Solid lines represent the joint theory fit, and dashed lines are individual Lorentzian fits to serve as a guide to the eye. Middle bottom, two-mode squeezing in red (antisqueezing in blue) calculated from the top panels as $\Delta_{\text{EPR}}^{\pm} = \bar{V}_{11} + \bar{V}_{33} \pm 2\bar{V}_{13}$. The darker-colored error bars represent the 2σ statistical error, and the outer (faint) 2σ error bars also include the systematic error in calibrating the added noise of the measurement setup.

detection noise floor $N_{j,\text{add}} + 0.5$, with the added noise $N_{e,\text{add}} = 13.1 \pm 0.4$ (2σ errors throughout) due to loss and amplifier noise and $N_{o,\text{add}} = 5.5 \pm 0.2$ due to optical losses, which were carefully determined using noise thermometry of a temperature-controlled $50\ \Omega$ load and four-port calibration, respectively (29). Because the emission bandwidth was smaller than the measurement bandwidth, the time domain measurement does not reveal the full SPDC amplitude.

We continued the analysis in the frequency domain by calculating the Fourier transform of each measurement for three separate time intervals: before ($2\ \mu\text{s}$), during ($200\ \text{ns}$), and immediately after ($500\ \text{ns}$) the entangling pump pulse. Figure 2D shows the resulting average microwave noise spectra for all three time intervals with corresponding fit curves (dashed lines) and theory (solid line). The spectra were in situ calibrated using the before-pulse off-resonance (waveguide noise) noise floor (29). Using independent measurements, we determined this noise floor $\bar{n}_{e,\text{wg}} = 0.001 \pm 0.002$

at the low average pump power of $\approx 0.12\ \mu\text{W}$ used in this experiment (29). Before and after the pump pulse, the intrinsic microwave bath occupancies were fitted to be $\bar{n}_{e,\text{int}} = 0.03 \pm 0.01$ and 0.09 ± 0.03 , respectively, above the vacuum level. Similarly, Fig. 2E shows the obtained average optical noise spectra during and after the pump pulse, calibrated through the shot noise level in the heterodyne measurement before the pulse. As expected, the optical noise level after the pulse returned back to the shot noise level.

During the pump pulse, approximately Lorentzian-shaped microwave and optical power spectra were generated through the SPDC process. A joint fit of the microwave and optical power spectral density during the pulse was performed using a five-mode theoretical model that includes the effects of measurement bandwidth. In this model, the in-pulse microwave bath occupancy $\bar{n}_{e,\text{int}} = 0.07 \pm 0.03$ and the cooperativity $C = 0.18 \pm 0.01$ are the only free fit parameters (29). The narrowed microwave linewidth $\kappa_{e,\text{eff}}/2\pi = 9.8 \pm 1.8\ \text{MHz}$

(taken from a Lorentzian fit) agrees with coherent electro-optical back-action (28). From the extracted numbers, we conclude that during the entanglement pulse, the quantum noise dominates the intrinsic microwave thermal noise, a prerequisite for microwave-optics entanglement generation.

The quadratures X_j and P_j were extracted as a function of frequency, i.e., at $\Delta\omega_j = \pm(\omega - \omega_j)$ around the resonances due to energy conservation in the SPDC process (29, 35) during the pump pulse. At each frequency, the bipartite Gaussian state of the propagating output fields was fully characterized by the 4×4 covariance matrix (CM) $V_{ij} = \langle \delta u_i \delta u_j + \delta u_i \delta u_j \rangle / 2$, where $\delta u_i = u_i - \langle u_i \rangle$ and $u \in \{X_e, P_e, X_o, P_o\}$ (29). The CM corresponds to the quantum state of the propagating fields in the coaxial line and the coupling prism at the device output, i.e., before setup losses or amplification incur. The diagonal elements in V correspond to the individual output field quadrature variances in dimensionless units, which can be obtained by subtracting the added detection

noise offsets from the measured variances, i.e., $V_{ii}(\Delta\omega) = V_{ii,\text{meas}}(\Delta\omega) - N_{i,\text{add}}$.

The obtained CM from the data in Fig. 2 at $\Delta\omega = 0$ is shown in Fig. 3A in its standard form (31, 32). The nonzero off-diagonal elements indicate strong correlations between microwave and optical quadratures. To verify the quantum correlation, the two-mode squeezed quadratures are more intuitively visualized in terms of the quasiprobability Wigner function:

$$W(\mathbf{u}) = \frac{\exp\left[-\frac{1}{2}\mathbf{u}V^{-1}\mathbf{u}^T\right]}{\pi^2\sqrt{\det(V)}} \quad (2)$$

where $\mathbf{u} = (X_e, P_e, X_o, P_o)$. Different marginals of this Wigner function are shown in Fig. 3B. The marginals from the same quadratures (X_e, P_e) and (X_o, P_o) show uncorrelated thermal noise above the vacuum noise (gray circle) from SPDC. The cross-quadrature marginals (X_e, X_o) and (P_e, P_o) show two-mode squeezing in the diagonal and off-diagonal directions below the vacuum level. The amount of squeezing was slightly different between the two because of the statistical uncertainty in the measured CM.

Figure 3C shows the amount of two-mode squeezing between microwave and optical output fields. The averaged microwave quadrature variance (purple dots) $\bar{V}_{11} = (V_{11} + V_{22})/2$ and the averaged optics quadrature variance (green dots) $\bar{V}_{33} = (V_{33} + V_{44})/2$ are shown in the top panel, along with the prediction from the five-mode theory (solid line) and a simple fit to a Lorentzian function (dashed line), which show perfect agreement. Measured microwave-optical correlations (yellow dots) $\bar{V}_{13} = (V_{13} - V_{24})/2$ and the Lorentzian fit (dashed line) lie slightly below the theoretical prediction (solid line), which we attribute to remaining imperfections in the phase stability (29).

The bottom two panels of Fig. 3C show the squeezed and antisqueezed joint quadrature variances $\Delta_{\text{EPR}}^{\pm} = \bar{V}_{11} + \bar{V}_{33} \mp 2\bar{V}_{13}$ (red and blue, respectively). We observed two-mode squeezing below the vacuum level, i.e., $\Delta_{\text{EPR}}^{-} < 1$, with a bandwidth close to the effective microwave linewidth. The maximal two-mode squeezing of $0.72_{-0.25}^{+0.31}$ dB is observed on resonance where $\Delta_{\text{EPR}}^{-} = 0.85_{-0.06}^{+0.05}$ (2σ , 95% confidence) obtained from ~ 1 million pulses with $\bar{V}_{11} = 0.93$, $\bar{V}_{33} = 0.84$, and $\bar{V}_{13} = 0.46$. The reported 2σ error on Δ_{EPR}^{-} takes both statistical and systematic errors into account. Thus, the value of Δ_{EPR}^{-} beats the classical limit ($\Delta_{\text{EPR}}^{-} = 1$) by $>5\sigma$ (29). The measured two-mode squeezing signifies an itinerant microwave-optical entangled state with a logarithmic negativity of $E_N = 0.17$. The supplementary materials contain additional data for longer pulses and varying optical pump power, which corroborate the presented results and findings (29).

Conclusions

The demonstration of deterministic quantum entanglement between propagating microwave and optical photons establishes a nonclassical communication channel between circuit quantum electrodynamics and quantum photonics. The achieved entanglement generation rate of ~ 0.11 ebits/200-ns-long pulse (29) is in practice limited by the slow pulse repetition rate. We expect orders-of-magnitude higher rates with improved thermalization, higher microwave and optical quality factors, and electro-optic coupling enhancements that reduce the required pump power and the associated thermal load. Coupling efficiency improvements will allow for higher levels of two-mode squeezing (29) and facilitate deterministic entanglement distribution schemes to qubits (29, 36), teleportation-based state transfer (21, 22, 29), and quantum-enhanced remote detection (37). This device and state preparation scheme can also be used directly for probabilistic heralding assisted protocols (7, 38, 39) when the cooperativity is somewhat reduced. This is the most promising way forward to mitigating optical setup losses and extending the entanglement to room-temperature fiber optics. Being fully compatible with superconducting qubits in a millikelvin environment, such a device will facilitate the integration of remote superconducting quantum processors into a single coherent optical quantum network. This is relevant not only for modularization and scaling (40, 41) but also for efficient cross-platform verification of classically intractable quantum processor results (42).

REFERENCES AND NOTES

1. F. Arute et al., *Nature* **574**, 505–510 (2019).
2. M. Zhong et al., *Nature* **517**, 177–180 (2015).
3. Y. Yu et al., *Nature* **578**, 240–245 (2020).
4. Z.-L. Xiang, S. Ashhab, J. Q. You, F. Nori, *Rev. Mod. Phys.* **85**, 623–653 (2013).
5. G. Kurizki et al., *Proc. Natl. Acad. Sci. U.S.A.* **112**, 3866–3873 (2015).
6. A. A. Clerk, K. W. Lehnert, P. Bertet, J. R. Petta, Y. Nakamura, *Nat. Phys.* **16**, 257–267 (2020).
7. L.-M. Duan, M. D. Lukin, J. I. Cirac, P. Zoller, *Nature* **414**, 413–418 (2001).
8. S.-H. Wei et al., *Laser Photonics Rev.* **16**, 2100219 (2022).
9. G. Burkard, T. D. Ladd, J. M. Nichol, A. Pan, J. R. Petta, arXiv:2112.08863 [cond-mat.mes-hall] (2021).
10. P. Magnard et al., *Phys. Rev. Lett.* **125**, 260502 (2020).
11. Y. Zhong et al., *Nature* **590**, 571–575 (2021).
12. X. Han, W. Fu, C.-L. Zou, L. Jiang, H. X. Tang, *Optica* **8**, 1050 (2021).
13. M. Mirhosseini, A. Sipahigil, M. Kalaee, O. Painter, *Nature* **588**, 599–603 (2020).
14. R. Sahu et al., *Nat. Commun.* **13**, 1276 (2022).
15. B. M. Brubaker et al., *Phys. Rev. X* **12**, 021062 (2022).
16. A. Kumar et al., *Nature* **615**, 614–619 (2023).
17. M. J. Weaver et al., arXiv:2210.15702 [quant-ph] (2022).
18. S. Takeda, T. Mizuta, M. Fuwa, P. van Loock, A. Furusawa, *Nature* **500**, 315–318 (2013).

19. K. G. Fedorov et al., *Sci. Adv.* **7**, eabk0891 (2021).
20. S. L. N. Hermans et al., *Nature* **605**, 663–668 (2022).
21. A. Rueda, W. Hease, S. Barzanjeh, J. M. Fink, *npj Quantum Inf.* **5**, 108 (2019).
22. J. Wu, C. Cui, L. Fan, Q. Zhuang, *Phys. Rev. Appl.* **16**, 064044 (2021).
23. U. L. Andersen, T. Gehring, C. Marquardt, G. Leuchs, *Phys. Scr.* **91**, 053001 (2016).
24. W. Hease et al., *PRX Quantum* **1**, 020315 (2020).
25. M. Tsang, *Phys. Rev. A* **81**, 063837 (2010).
26. V. S. Ilchenko, A. A. Savchenkov, A. B. Matsko, L. Maleki, *J. Opt. Soc. Am. B* **20**, 333 (2003).
27. L. Fan et al., *Sci. Adv.* **4**, eaar4994 (2018).
28. L. Qiu, R. Sahu, W. Hease, G. Arnold, J. M. Fink, arXiv:2210.12443 [quant-ph] (2022).
29. See the supplementary materials.
30. A. Einstein, B. Podolsky, N. Rosen, *Phys. Rev.* **47**, 777–780 (1935).
31. L.-M. Duan, G. Giedke, J. I. Cirac, P. Zoller, *Phys. Rev. Lett.* **84**, 2722–2725 (2000).
32. R. Simon, *Phys. Rev. Lett.* **84**, 2726–2729 (2000).
33. Z. Y. Ou, S. F. Pereira, H. J. Kimble, K. C. Peng, *Phys. Rev. Lett.* **68**, 3663–3666 (1992).
34. H. Bernien et al., *Nature* **497**, 86–90 (2013).
35. S. Zippilli, G. D. Giuseppe, D. Vitali, *New J. Phys.* **17**, 043025 (2015).
36. J. Ang et al., *Phys. Rev. A* **105**, 062454 (2022).
37. S. Barzanjeh et al., *Phys. Rev. Lett.* **114**, 080503 (2015).
38. C. Zhong et al., *Phys. Rev. Lett.* **124**, 010511 (2020).
39. S. Krastanov et al., *Phys. Rev. Lett.* **127**, 040503 (2021).
40. S. Bravyi, O. Dial, J. M. Gambetta, D. Gil, Z. Nazario, *J. Appl. Phys.* **132**, 160902 (2022).
41. J. Ang et al., arXiv:2212.06167 [quant-ph] (2022).
42. J. Knörzer, D. Malz, J. I. Cirac, arXiv:2212.07789 [quant-ph] (2022).
43. R. Sahu, Data for: Entangling microwaves with light, Zenodo; <https://doi.org/10.5281/zenodo.7789418>.

ACKNOWLEDGMENTS

L.Q. thanks J. Li and D. Vitali for fruitful discussions. **Funding:** This work was supported by the European Research Council (grant no. 758053, ERC StG QUNNECT) and the European Union's Horizon 2020 Research and Innovation Program (grant no. 899354, FETopen SuperQULAN). L.Q. acknowledges generous support from the ISTFELLOW program. W.H. is the recipient of an ISTplus postdoctoral fellowship with funding from the European Union's Horizon 2020 Research and Innovation Program (Marie Skłodowska-Curie grant no. 754411). G.A. is the recipient of a DOC fellowship of the Austrian Academy of Sciences at IST Austria. J.M.F. acknowledges support from the Austrian Science Fund (FWF) through BeyondC (grant no. F7105) and the European Union's Horizon 2020 Research and Innovation Program (grant no. 862644, FETopen QUARTET). **Author contributions:** R.S., W.H., L.Q., and G.A. worked on the experimental setup. R.S. and L.Q. performed the measurements. L.Q. and R.S. analyzed the data. L.Q. developed the theory with contributions from R.S., Y.M., and P.R. R.S. and L.Q. wrote the manuscript with contributions from all authors. J.M.F. supervised the project. **Competing interests:** The authors declare no competing interests. **Data and materials availability:** All data are available in the manuscript or the supplementary materials or have been deposited on Zenodo (43). **License information:** Copyright © 2023 the authors, some rights reserved; exclusive licensee American Association for the Advancement of Science. No claim to original US government works. <https://www.science.org/about/science-licenses-journal-article-reuse>

SUPPLEMENTARY MATERIALS

science.org/doi/10.1126/science.adg3812
Supplementary Text
Figs. S1 to S15
Tables S1 and S2
References (44–54)

Submitted 20 December 2022; accepted 19 April 2023
10.1126/science.adg3812